3D-Printed Synthetic Hydroxyapatite Scaffold With In Silico Optimized Macrostructure Enhances Bone Formation In Vivo

Dorien Van hede[*]*, Bingbing Liang, Sandy Anania, Mojtaba Barzegari, Bruno Verlée, Grégory Nolens, Justine Pirson, Liesbet Geris, France Lambert*

Dr. D. Van hede
Department of Periodontology, Oral Surgery and Implant Surgery, Faculty of Medicine, University Hospital of Liège
Dental Biomaterials Research Unit, Faculty of Medicine, University of Liège
Avenue de l'Hôpital 1, 4000 Liège, Belgium

B.Liang
Biomechanics Research Unit, GIGA In silico Medicine, University of Liège, Belgium
Avenue de l'Hôpital 1, 4000 Liège, Belgium

S. Anania
Dental Biomaterials Research Unit, Faculty of Medicine, University of Liège
Metastasis Research Laboratory (MRL), GIGA-Cancer, Pathology Institute B23, University of Liège
Avenue de l'Hôpital 1, 4000 Liège, Belgium

M. Barzegari
Biomechanics Section, Department of Mechanical Engineering, KU Leuven
Celestijnenlaan 300, B-3001 Heverlee (Leuven), Belgium

B.Verlée
Department of Additive Manufacturing, Sirris Liège
Rue du Bois Saint-Jean 12, 4102 Seraing, Belgium

Dr G. Nolens
Faculty of Medicine, University of Namur
Place du Palais de Justice 175, 5000 Namur, Belgium

J. Pirson
Wishbone SA
Rue de l'Expansion 1/3, 4400 Flemalle, Belgium

Prof. L. Geris
Biomechanics Research Unit, GIGA In silico Medicine, University of Liège
Biomechanics Section, Department of Mechanical Engineering, KU Leuven
Skeletal Biology and Engineering Center, KU Leuven
Avenue de l'Hôpital 1, 4000 Liège, Belgium

Prof. L. Lambert
Department of Periodontology, Oral Surgery and Implant Surgery, Faculty of Medicine, University Hospital of Liège
Dental Biomaterials Research Unit, Faculty of Medicine, University of Liège
Avenue de l'Hôpital 1, 4000 Liège, Belgium

Keywords: computer modelling, stereolithography, calcium phosphate scaffold, bone regeneration, nanofocus computed tomography, histology, intra-oral defects

Abstract

3D printing technologies are a promising approach to treat intra-oral bone defects, especially those with poor regenerative potential. However, there is a lack of evidence regarding the impact of internal design specifications on the bone regenerative potential. Here, we propose an in silico approach to optimize the internal design of calcium-phosphate based scaffolds for bone regeneration. Based on an in silico model of neotissue formation, a Gyroid 3D-printed scaffold was designed and manufactured using UV stereolithography of bioceramic materials. An orthogonal lattice structure 3D-printed scaffold and a particulate xenograft were used as control groups. The scaffolds were implanted subperiosteally under a shell on rat calvarium for 4 or 8 weeks and bone neoformation performances were investigated by Nanofocus Computed Tomography and decalcified histology. After 8 weeks, the Gyroid group was associated with a higher ingrowth potential of the bone and was characterized by signs of osteoinduction (newly formed bone islands). The bone to material contact was similar between the Gyroid and the particulate groups. The present results reinforce this in silico modelling strategy to design calcium phosphate-based 3D scaffolds and the gyroid experimental internal architecture seems to be highly promising for intra-oral bone regeneration applications.

1. Introduction

Despite being very common, intra-oral bone defects are still challenging clinical situations that can be lengthy to treat with often unpredictable outcomes owing to the lack of patient-customized treatment. Although particulate bone substitutes have demonstrated their efficacy in self-containing defects, they have shown limitation inherent to their lack in 3-dimensional (3D) stability in defects with poor regenerative potential. Alternatively, blocks of different sources (autologous or allogeneic cortical bone, xenogeneic and synthetic bone blocks) were

tested in animals and humans with most of them displaying the main disadvantages of being shaped by hand to fit the patient's bone defect and containing no or inappropriate interconnectivity for neovascularization, reducing their overall bone regenerative performances.[1–6] Nowadays, combination of several new technologies such as Computer-Aided Design - Computer-Aided Manufacturing (CAD-CAM), Cone Beam Computed Tomography (CBCT) and high resolution stereolithograhy (SLA),[7–11] enable the fabrication of patient-customized 3D scaffolds with tailored dimensions, shape and internal design.[12–15]

The internal design together with the surface properties are two major factors influencing bone regeneration performances of 3D-printed scaffolds.[16–20] Whereas the surface roughness depends on biomaterial composition and postproduction processes (sintering t°, coatings,…), [21,22] recent 3D printing technologies allow the manufacturing of custom-made scaffolds with a multitude of internal design. In silico modelling (the use of computer modeling and simulation) is a key approach to avoid the in vivo testing of numerous designs, in accordance with the 3 R's principle, by designing and selecting the most promising patterns according to the predictions established by the model. As the efficacy of bone regeneration is dependent of a number of parameters, the ideal model should consider as many of them as possible. Besides the well-studied factors (biochemical, physical and surface properties), the effect of the 3D scaffold internal design is less explored although this parameter has an important impact on the tissue formation rate.[23–27] A variety of in silico bone regeneration models has been proposed in the literature,[28] with most of them corroborated by comparison with historic or dedicated animal experiments. However, most of them focus either on scaffold-free regeneration [29] or a specific shape [30–32] rather than using the model to optimize the scaffold structure. In silico models focusing on optimizing scaffold internal design to maximize neotissue formation have primarily been corroborated by in vitro 3D cell culture experiments.[25,33]

Previously, we developed an SLA-based approach to fabricate 3D-printed synthetic CaP scaffolds aiming to generate new bone while being biocompatible.[34] Our proof-of-concept was

challenged in a subperiosteal cranial rat model using 3D-printed pellets displaying a simple macrostructure (rounded unidirectional channels). Although biocompatibility and biological performance were demonstrated, the tested scaffolds did not explore different 3D geometries. Based on the in silico modelling and using high resolution SLA 3D printers, the present study goes one step forward investigating the effect of complex and optimized scaffold on bone regeneration.

The objective of the present study was to reinforce our in silico modelling strategy by evaluating the in vivo biological performances of our optimized 3D-printed scaffold (Gyroid) in a small animal bone augmentation model compared to a gold standard (granules of Bio-Oss) and a classic geometry (Orthogonal).

2. Results

2.1. In silico modelling

Neotissue growth was simulated for a variety of lattice-based and Triply Periodic Minimal Surface (TPMS) structures. The gyroid-TPMS showed most promising neotissue formation due to its favourable local curvature. In a second round of in silico modelling, the gyroid structure was further investigated in terms of its pore size and wall thickness, in order to obtain the combination leading to optimal neotissue growth. Pore size was varied between 700 µm and 1.3 mm and wall thickness was varied from 200 µm to 800 µm **(Figure 1)**, which are ranges that take into account restrictions of the manufacturing process in terms of smallest feature dimensions. Balancing the need for swift neotissue ingrowth **(Figure 1B, relevant for short-term implant stability)** with the volume of neotissue formed (Figure 1A, relevant for long-term implant stability), the combination of 700 µm pore size and 200 µm wall thickness **(Figure 1C)** was chosen as the optimal structure to continue with the experimental part of this study.

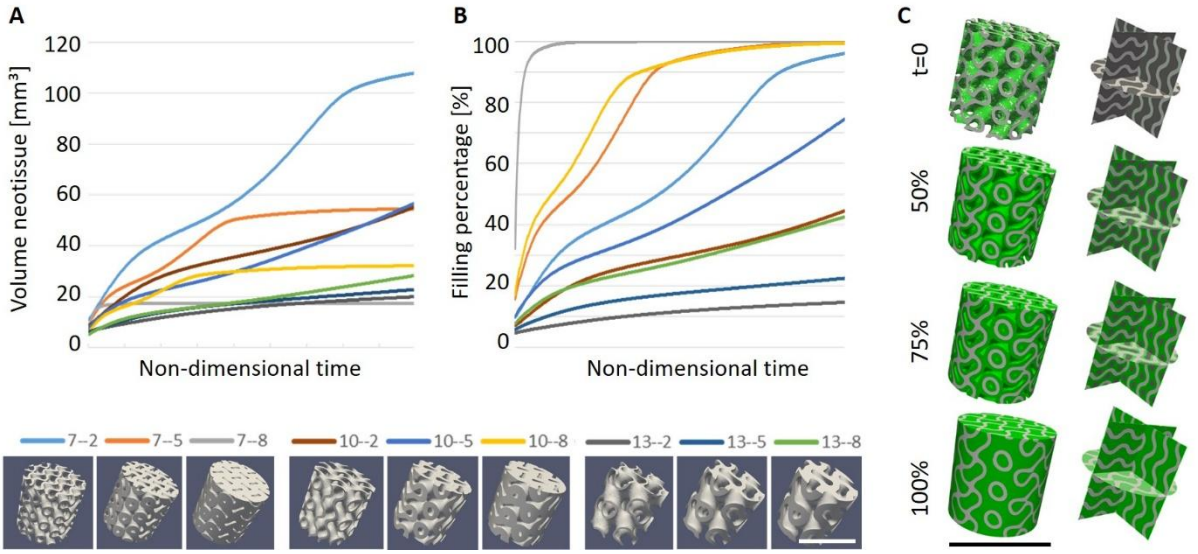

Figure 1. In silico predictions of neotissue formation. Neotissue formation quantified in absolute volume (A) and filling percentage (B) for cylindrical test samples (ø 6 mm, height 6 mm). The different combinations are indicated in the legend by 2 numbers, the first of which refers to pore size (7: 700 µm, 10: 1 mm, 13: 1.3 mm) and the second refers to wall thickness (2: 200 µm; 5: 500 µm; 8: 800 µm;). (C) Side view and cross-sectional view of neotissue growth in gyroid (7-2) scaffold for different levels of filling, starting with initial condition at t=0 (top). Scale bars: 6 mm

2.2. Physico-chemical characterization

Orthogonal and Gyroid inserts were composed of approximatively 94% of Ca5(PO4)3(OH) (hydroxylapatite) and 6% of β-Ca3(PO4)2 (β-TCP) whereas α-Ca3(PO4)2 (α-TCP) was undetectable. From a qualitative point of view, SEM analysis revealed similar surface roughness of both 3D-printed scaffolds whereas more microporosities were observed for the Granules group **(Figure 2)**.

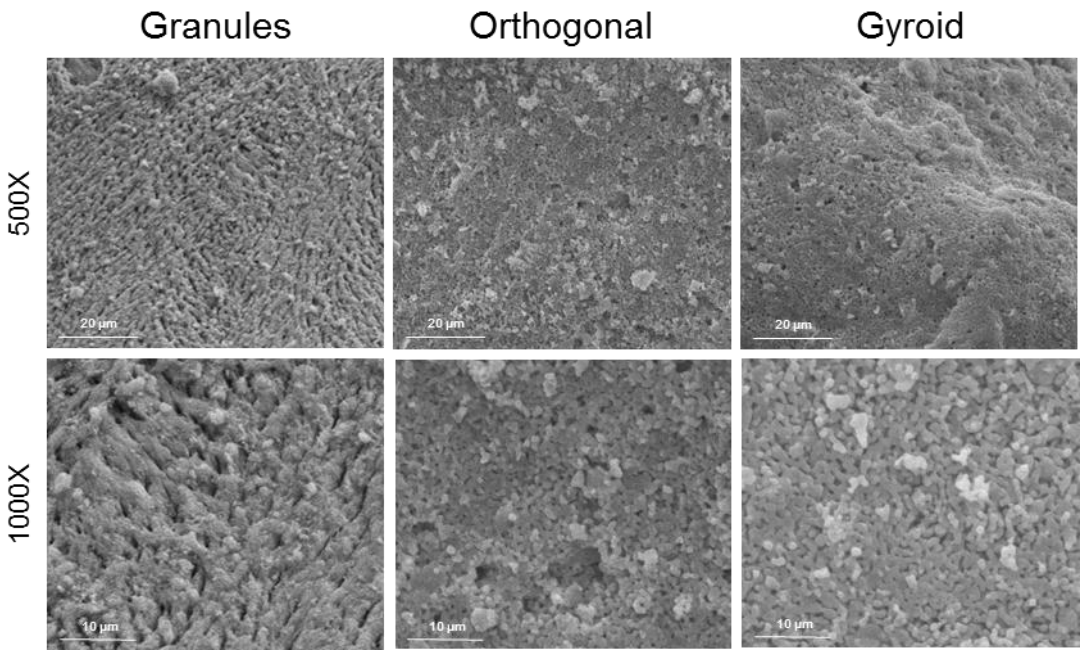

Figure 2. Scanning Electron Microscopy analysis. Surface topographies of the three biomaterials are shown at low (500X) and high (1000X) magnifications.

2.3. In vivo implementation

2.3.1. Nano-CT analysis

The percentage of newly formed bone (Bone) within the Total Volume (VOI1) was similar between the 3 groups at 4 weeks but was higher in the Gyroid group at 8 weeks compared to the Granules and the Orthogonal groups ($p < 0.0001$) **(Figure 3A)**. Moreover, the percentage of Bone increased with time for the Granules ($p < 0.05$) and the Gyroid ($p < 0.0001$) groups but was stable for the Orthogonal group. Additional output measures were carried out but did not change the overall conclusion **(Supplementary Materials)**. At 8 weeks, the highest point of Bone was superior for the Gyroid group compared to the Granules and the Orthogonal groups ($p < 0.0001$) **(Figure 3B)**. Moreover, at 4 and 8 weeks, it was higher for the Orthogonal group compared to the Granules group ($p < 0.05$). This parameter did not evolve with time in the Granules and the Orthogonal groups but increased in the Gyroid group ($p < 0.0001$). Interestingly, when looking at these highest points of newly formed bone within the 3D-printed scaffolds, we observed that most of them formed self-standing islets of bone, in the Gyroid group in particular.

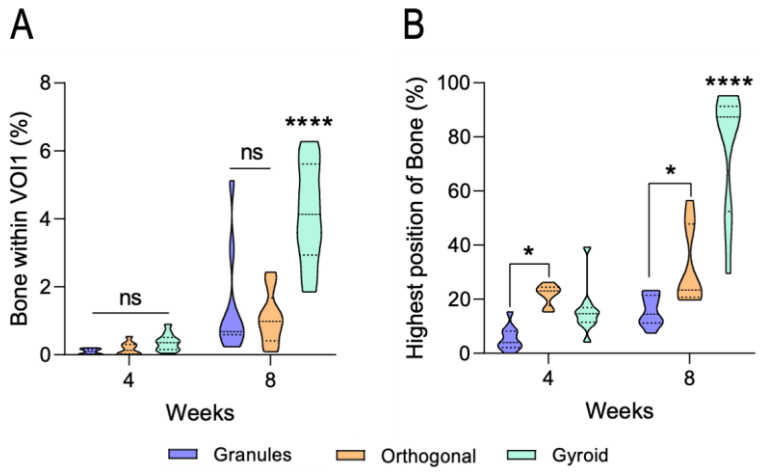

Figure 3. Bone regeneration analysis by Nano-CT. The percentages of newly formed bone between the Granules, the Orthogonal and the Gyroid groups were determined within the VOI1 (A) at 4 and 8 weeks. The bone highest position was calculated at 4 and 8 weeks (B). ns = not significant; * = $p < 0.05$; **** = $p < 0.0001$.

2.3.2. Histological descriptive analysis and Bone to Material Contact (BMC)

At 4 weeks, the scaffolds in all three groups were mainly colonized by soft tissues. Remaining blood clots were observed mostly in the centre and the highest areas of the scaffolds. Blood vessels were present in each sample but more and larger ones were observed in the 3D-printed scaffolds. Few inflammatory cells were noticed in some samples. Early bone colonization, characterized by woven bone and starting from the calvarium, was observed in all the 3D-printed samples but only in some of the Granules group. At 8 weeks, the amount of bone inside the scaffolds increased, especially in the 3D-printed scaffolds. Moreover, islets of bone were observed at the distal portion of the scaffold in almost all Gyroid group samples. Overall, no major signs of inflammation were highlighted among the investigated groups **(Figure 4)**.

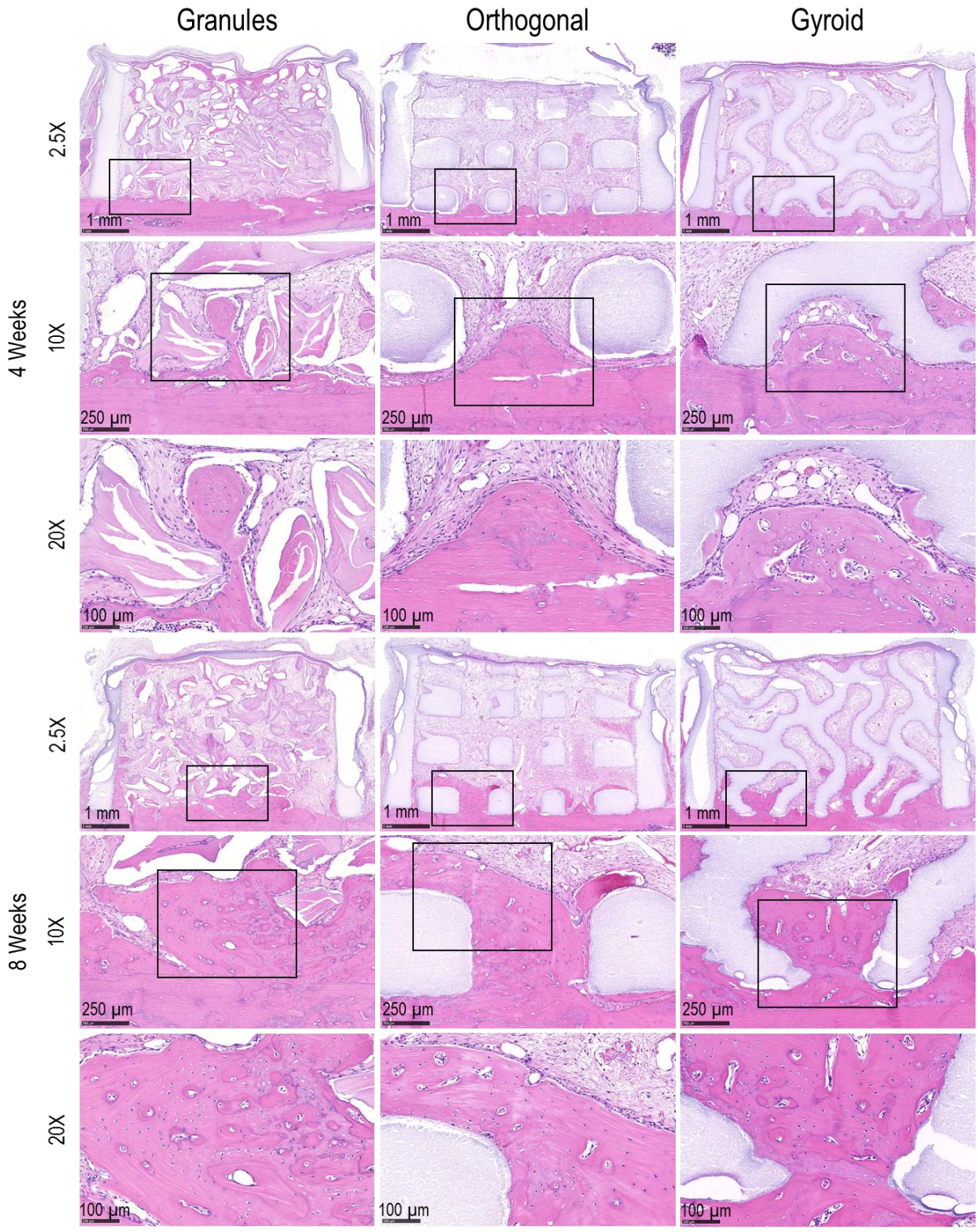

Figure 4. Representative histological sections from the three experimental groups at 4 and 8 weeks. At 4 weeks post-implantation, the low magnification pictures (2.5X) allowed to visualize a low, localized but similar new bone formation between each of the three experimental groups. At 8 weeks, bone formation was still localized in the Granules group whereas the 3D-printed scaffolds displayed a widespread bone colonization (low magnification pictures). At higher magnification (20X), large blood vessels were observed to be increasingly present in the 3D-printed scaffolds.

As the Nano-CT analysis revealed weak rates of bone regeneration and highlighted no difference between the groups at 4 weeks, the BMC was not determined for this time point. At 8 weeks, the BMC was superior for the Gyroid group compared to the Orthogonal group ($p < 0.05$), with a distribution between approximatively 30 and 50%, and a median of 40%, whereas the Orthogonal group displayed a more scattered distribution (10 to 50%) and a median inferior to 20%. No difference between the Granules and the Gyroid groups was highlighted **(Figure 5)**.

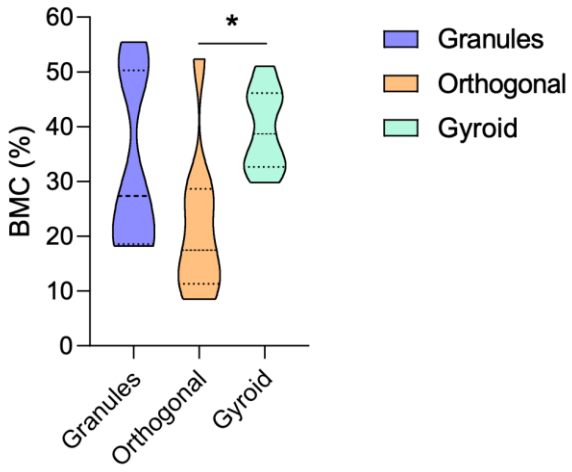

Figure 5. The Bone to Material Contact (BMC) at 8 weeks. The percentages of Bone to Material Contact (BMC) were calculated using the 8 weeks histological sections. * = $p < 0.05$.

3. Discussion

This study demonstrates that our 3D-printed HA scaffolds with in silico-optimized internal macro-porous architecture (Gyroid group) enhanced bone neoformation in a subperiosteal bone augmentation calvarial rat model and, therefore, corroborates the in silico model in its qualitative prediction of neotissue growth acceleration between different structures. Although the scaffolds from the 3 groups showed similar mineral composition and surface roughness, in vivo results highlighted a superior bone regenerative potential in the in silico optimized gyroid group (amount and height).

In silico modelling is widely used for tissue engineering as it offers a more exhaustive approach compared to a "trial-and-error" method and reduce the number of experimental tests. Optimization of scaffold structures for bone tissue engineering purposes is often corroborated by comparison with in vitro tests [25,33] and only a small number of in vivo studies have been reported.[35–37] However, in these in vivo studies, optimization was firstly performed on mechanical properties rather than the structural elements such as local curvature underlying the in silico model used this study.

HA was chosen to fabricate the 3D-printed scaffolds because among the various CaP ceramics, HA is the least soluble, providing a long term 3D stability of the regeneration, and is known to be highly biocompatible as its composition is similar to the natural bone matrix.[38] Thanks to its different properties, this CaP ceramic is a widely used synthetic bone substitute for bone regeneration procedures.[39] Nano-CT and histological analysis of the in vivo ectopic implantation data showed that none of the scaffolds underwent a substantial resorption over the experimentation follow-up period as expected from the HA material used in this study. [38] The physico-chemical analyses showed that, in all experimental 3D-printed scaffolds, a small portion of HA (6%) was transformed in β-TCP which is most likely induced by the sintering process. The presence of β-TCP, being more soluble, may actually play a role in the regenerative process by releasing Ca+ ions in the environment and contribute to the bone forming process.[40] The relatively low sintering temperature used in the present study allowed to produce experimental scaffolds with a surface topography rather close to the natural bone surface characteristics favourable for cell adhesion, anchoring and proliferation.[34,41,42]

In vivo results obtained from the Nano-CT analysis highlighted the superior bone regenerative potential of the gyroid design with more newly formed bone inside the scaffold, especially in the highest parts of the scaffolds. This result emphasized, besides the pore size parameter, the critical role of the pore geometry and orientation when designing 3D scaffolds for bone regeneration applications.[43–45] Indeed, whereas cell growth preferentially occurred within

highly curved pore corners, tissue growth is favoured within pores displaying numerous corners such as hexagons compared to rectangular and triangular pores.[43] Moreover, pore orientation may also influence bone regeneration. [46–48] The orientation of the gyroid structure, with waved channels running from the parietal bone to the top of the insert, might have allowed for a curvotaxis-type of migration of progenitors into the insert.[49] Finally, the screening of the 3D volumes of each sample revealed the presence of independent bone islets in most of the 8 weeks Gyroid samples solely. This observation may suggest that this particular design harbour some osteoinductive capacity which is in accordance with previous works highlighting the effect of pore interconnectivity on bone ingrowth.[48,50,51] Additionally, having even isolated islands of bone formation at all levels throughout the implant scaffold, will be beneficial for follow-up actions such as oral implant osseointegration.

The histological analysis revealed no signs of inflammatory reactions neither at 4 weeks nor at 8 weeks of implantation in any of the three experimental groups, indicating that the manufacturing process and post-manufacturing treatment produced biocompatible 3D-printed scaffolds as previously described.[34] On the other hand, histological sections showed the presence of more and larger blood vessels within the 3D-printed scaffolds compared to the Granules group. This observation highlights the importance of internal design to improve bone regeneration through an enhanced neovascularization. Indeed, previous reports indicated that optimal blood vessels neoformation occurs in macro-pores characterized by a diameter ranging from 100 to 800 μm, depending on the experimental conditions. [52–56]

Finally, the interface between the newly formed bone and the biomaterial surface (BMC) was equivalent in the Gyroid and the Granules groups while less contact was found in the Orthogonal group. If surface topography was often correlated to the degree of osseointegration of regenerative materials, [19,21,57] the present results suggest that additional characteristics such as the pore size, geometry and orientation may also play a role in the osteoconduction process.

Taken together, the present results emphasize the excellent biological performances of the 3D-printed scaffolds and the better performance of the gyroid design supporting the role that in silico modelling can play in designing optimized macro-porous architectures of cell-free scaffolds for bone regeneration.

However, our study encounters some limitations that should be underlined. Simulation results have been used in a qualitative way after the curvature-based growth principle was confirmed in dedicated in vitro tests but without aiming to provide a detailed quantitative prediction of the actual in vivo experiment. Using the proposed in silico model in a quantitative way requires a substantial amount of data to fully validate the model. [58–60] The experimental results generated in this study can now serve to further validate the in silico model so that it can develop into a stand-alone tool for quantitative in vivo neotissue formation prediction. For manufacturing reasons, while pore diameter was standardized, pore struts differed between the 3D-printed scaffolds, leading to Orthogonal scaffolds with larger struts and thus fewer empty spaces for bone neoformation compared to the Gyroid group. This limitation was mitigated by normalizing the VOI2 in each group using the VOI2 of the Granules group as reference **(Supplementary materials)**. Because of the global dimensions of the scaffolds, it was not possible to implant more than one scaffold per animal, resulting in an uncontrolled inter-animal variation. However, this weakness was compensated by the high study power (n=10 for every time point in every group). Finally, and in order to enhance the standardization of the animal experimentation, instead of the usual collagen barrier membrane, a rigid HA-based shell was used to limit the ingrowth of soft tissue into the scaffold. However, this is not fully representative of the clinical application and similar experiments on bigger animals would be necessary in order to validate such a treatment concept in more realistic conditions.

4. Conclusion

Within the limits of the present study, we demonstrated that in silico model facilitates the internal design optimization of 3D-printed scaffolds for bone regeneration applications. The Gyroid design, identified using in silico modelling, displayed better regenerative performance compared to the gold standard or the orthogonal printed structures. Further developments in larger animal models are however necessary to translate this concept to clinical practice.

5. Experimental section

5.1. In silico scaffolds design

In order to define the optimal scaffold geometry leading to maximal neotissue formation, a previously developed in silico model of neotissue growth was used. [61] Full details are provided in the supplementary materials. Briefly, neotissue growth in porous scaffolds has been shown to be depending on the local mean curvature of the interface between the scaffold and the neotissue.[26,62] The in silico model uses the Level Set Method to implement this curvature-based growth through a simulation of the movement of the interface between the neotissue and the void space. The speed of the moving interface is made dependent on the mean local curvature, leading to an effective and efficient implementation of the curvature-based growth.[61] The model calibration performed in Guyot et al. was for Titanium scaffolds culture in a bioreactor setting.[61] For the purpose of the present study, dedicated calibration experiments were performed on prismatic structures, demonstrating a considerably slower growth on the CaP scaffolds, nevertheless confirming the curvature-based nature of the growth. Neotissue growth was then simulated for a variety of lattice-based structures as well as structures from the TPMS family **(Figure 6B-C)** and compared in a qualitative way. A full quantitative prediction is not possible due to the absence of relevant validation experiments, which explains why comparisons between geometries are made over non-dimensional time. After identification of the gyroid-TMPS as the optimal structure, an additional analysis was carried out to investigate the pore size and wall thickness best suited to stimulate neotissue

ingrowth by maximizing speed of growth as well as amount of neotissue formed, while taking into account restrictions of the manufacturing process in terms of smallest feature dimensions. The gyroid scaffold identified through this process was manufactured along with a lattice-based control.

5.2. Scaffold manufacturing

Orthogonal and Gyroid inserts as well as shells were implemented in Netfabb by Autodesk **(Figure 6A-C)**. They were produced using a SLA machine (Prodways V6000, France) and composed of hydroxyapatite as previously described **(Figure 6D-F)**.[34] Briefly, the bioceramic was carefully mixed with organic components (polyfunctional acrylic resins and UV-photoinitiator) in order to obtain a viscous paste material to be processed by SLA (Cerhum and Sirris, Belgium). The solid loading was about 50% for both formulations. During the process, the suspension was spread on the working area in thin layers of 50 μm. After spreading a layer, UV-light was projected by a DLP (Digital Light Processing) on the paste surface. The samples were then submitted to a thermal cycle (1125°C, for 5hr) allowing the removal of the resin and the densification of the ceramic.[63] After manufacturing, the parts were rinsed and ultrasonically cleaned in an ethanol 80% bath for 10 min. As a final step, they underwent an autoclave sterilization (134°C for 30 min) before in vivo implantation.

5.3. Physico-chemical characterization

Gyroids and orthogonal parts were analysed using a diffractometer (Rigaku Miniflex 600) in order to identify and quantify their mineralogical phases. Moreover, a qualitative analysis of their surface microtopography was carried out with a scanning electron microscope (SEM). Scaffolds were mounted on SEM stubs and coated with platinum using a Q 150T S sputter coater (Quorum Technologies, West Sussex, UK). The sample surface analysis was performed using a QuantaTM 250 FEG-SEM.

5.4. In vivo implantation

5.4.1. Animals and study design

Subperiosteal implantation of the scaffolds was performed in a calvaria rat model in order to determine the impact of the scaffold internal design on the bone augmentation performances in vivo. All experimental procedures used in this investigation were reviewed and approved by the Institutional Animal Care and Use Ethics Committee of the University of Liège, Belgium (ethical number 1527). Animal Research Reporting of In Vivo Experiments guidelines were carefully followed as well as national and European legislation.[64] The male Wistar rats were acquired from the University of Liège and randomly allocated into 6 groups (three experimental scaffolds: Granules, Orthogonal and Gyroid; two time points: 4 and 8 weeks).

5.4.2. Global scaffold design

Scaffolds were produced in two parts, an insert (3.4 mm in length, 5,1 mm in width and 4 mm in height) and a shell (6.5 mm in length, 5 mm in width and 5 mm in height, 0,7 mm wall thickness), with their respective dimensions allowing a perfect assembly of the insert into the shell. To play the role of a barrier and allow bone ingrowth exclusively from the calvarium, the shell was not perforated **(Figure 6A-F).** In addition, both inserts and shells displayed a slight curvature on their lower side to best fit the animal's skull. Shell design was identical for the 3 groups both types of scaffolds. The insert designs corresponded to a lattice structure with square struts (Orthogonal group, pores diameter of 700 µm) or a gyroid structure (Gyroid group, pores diameter of 700 µm) while in the granule group the particles diameter ranged from 0.25 to 1 mm (Bio-Oss, Geistlich, Wolhusen, Switzerland).

5.4.3. Surgical procedure

Animals were anaesthetized with a combination of Ketamine (8 mg/kg) and Xylasine (5 mg/kg) administered intraperitoneally, the surgical site was shaved and few blood drops were collected from the tail extremity. Following a local administration of anesthetic (Septanest special,

Septodont, France), an antero-posterior incision was performed on the calvarium. A full thickness skin flap was raised in order to exhibit the entire parietal bone **(Figure 6G)**. Before implantation, the Bio-Oss particles were mixed with the collected blood while the inserts were filled in with it. The experimental specimens were then placed into a shell and a single scaffold was implanted over the sagittal calvarial suture in each animal according to the randomization **(Figure 6H)**. The surgical site was sutured with polypropylene 5/0 (Permashap, Hu Freidy, USA) **(Figure 6I)**. Antibiotics (Baytril, 5 mg/kg), painkillers (Temgésic, 0.05 mg/kg) and anti-inflammatory (Rimadyl, 5 mg/kg) drugs were administrated subcutaneously. After 4 and 8 weeks, rats were euthanized by an overdose of pentobarbital (Euthasol). The samples were harvested and fixed for 24 hours in 4% formaldehyde and then stored in PBS at 4°C until Nano-CT acquisition.

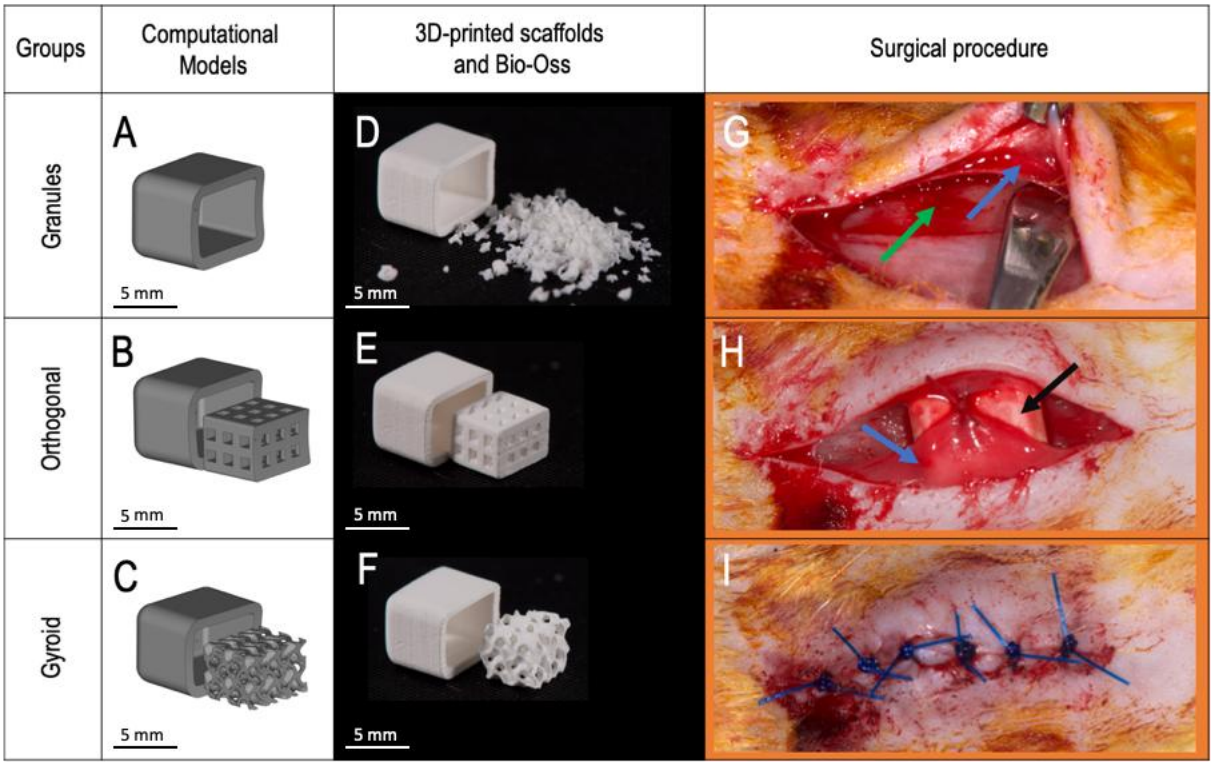

Figure 6. 3D designs based on the computational model, 3D-printed parts and surgical procedure. (A – C) Gyroid structures were suggested by the in silico model and compared to a lattice-based orthogonal structure and the clinical gold standard. (D – F) Shells and inserts were printed by stereolithography. (G – I) The surgical procedure is depicted. Blue arrows: detached periost; green arrow: parietal bone; black arrow: scaffold.

5.4.4 Nanofocus Computed Tomography (Nano-CT)

Nano-CT scans of the samples were acquired using the GE Phoenix Nanotom (Hawker Richardson, New Zealand). Scanning was carried out at 75 kV, 140 µA and with a 0.5 mm Aluminium filter. A total of 1800 images were taken over a 360° scan using the fast scan mode with a resolution of 5.5 µm per voxel. Scans 3D reconstruction was performed using Phoenix datos|x CT and then reoriented adequately with DataViewer (Bruker micro-CT, Kontich). Using the same software, the experimental inserts were selected excluding the shell. The selected volume (Total Volume, VOI1) was then quantitatively analysed with CTAn (Bruker micro-CT, Kontich). The quantity of newly formed bone was determined using a segmentation based on the grey levels. The percentage of bone was then calculated within the VOI1 as follows:

$$\text{Bone within VOI1 (\%)} = \frac{\text{Volume of Bone}}{\text{VOI1}} \text{ x } 100$$

Additional methodologies for bone volume quantification are presented in the supplementary materials.

As not only the quantity of bone but also the ingrowth into the scaffold is of importance, the distance between the parietal bone and the highest point of newly formed bone within the 3D scaffolds was measured in all samples as follows:

$$\text{\%} = \frac{\text{Highest point of Bone}}{\text{Total height of the scaffold}} \text{ x } 100$$

5.4.5. Qualitative histological analysis and Bone to Material Contact calculation

Following a decalcification procedure of two days using a mixture of hydrochloric acids (DC2, VWR,USA), the samples were embedded in paraffin. Five µm-thick longitudinal sections were obtained from three different levels of the samples and stained with hematoxylin and eosin. The histological sections were then scanned (NDP NanoZoomer Digital Pathology, Hamamatsu, Japan) and a descriptive analysis was performed (NDPView2, Hamamatsu).

Additionally, for the 8 weeks samples, the percentage of Bone to Material Contact (BMC) was calculated in areas where newly formed bone was present as follows:

$$\text{BMC (\%)} = \frac{\text{Perimeter of Biomaterial in contact with Bone}}{\text{Total Perimeter of Biomaterial}} \text{ x } 100$$

5.5. Statistical analysis

5.5.1. Sample size calculation

The required sample size was determined using the software Gpower. [65] The effect size was set at 0.55 and the power at 0.95. Thus, the calculated total sample size was 55 but it was rounded up to 60 according to the study design (6 groups with 10 animals per group).

5.5.2. Statistical tests

Statistical tests were carried out using GraphPad 8.3.0. Normality tests (D'Agostino & Pearson) were performed following outliers' identification (ROUT test with Q = 1%) and withdrawal. The percentage of Bone to Material Contact (BMC) was analysed using a One-Way ANOVA whereas a Mixed-effect model (REML) was used to analyse the % of Bone within the VOI1 and the highest point of newly formed bone. Tukey's and Sidak's corrections were applied for multiple comparisons. The data were presented as violin plots with quartiles and medians.

Supporting Information

Supporting Information is available from the Wiley Online Library or from the author.

Acknowledgements

This work was supported by the Walloon Region (BioWin project BIOPTOS: Convention n°7560), the Fund for Scientific Research Belgium FNRS (PDR T.0256.16) and the European Union's Horizon 2020 research and innovation programme via the European Research Council (ERC CoG INSITE 772418). We are grateful to the members of the Animal Facilities of the GIGA, ULiège (Prof. Pierre-Vincent Drion and Mr. Luc Duwez) and to the Immunohistology platform (Dr. Chantal Humblet) for technical and histological assistance as well as Dr. Philippe Compère for his help with SEM analysis. Finally, we thank the Department of Development and Regeneration of the KU Leuven (Mrs. Carla Geeroms) financed by the Hercules Foundation (project AKUL/13/47) for generating the Nano-CT images.

Received: ((will be filled in by the editorial staff))
Revised: ((will be filled in by the editorial staff))
Published online: ((will be filled in by the editorial staff))

Conflict of Interest

The authors declare they have no conflict of interests.

References

[1] J.-P. Carrel, A. Wiskott, S. Scherrer, S. Durual, *Clin Implant Dent Relat Res* **2016**, *18*, 1183.
[2] A. Giuliani, A. Manescu, S. Mohammadi, S. Mazzoni, A. Piattelli, F. Mangano, G. Iezzi, C. Mangano, *Implant Dent* **2016**, *25*, 6.
[3] K. Sawada, K. Nakahara, M. Haga-Tsujimura, T. Iizuka, M. Fujioka-Kobayashi, K. Igarashi, N. Saulacic, *Odontology* **2018**.
[4] L. Venet, M. Perriat, F. G. Mangano, T. Fortin, *BMC Oral Health* **2017**, *17*, 146.
[5] Z. Artzi, C. E. Nemcovsky, D. Dayan, *Clin Oral Implants Res* **2002**, *13*, 420.
[6] R. Spin-Neto, A. Stavropoulos, F. L. Coletti, L. A. V. D. Pereira, E. Marcantonio, A. Wenzel, *Clin Oral Implants Res* **2015**, *26*, 747.
[7] M. Figliuzzi, F. G. Mangano, L. Fortunato, R. De Fazio, A. Macchi, G. Iezzi, A. Piattelli, C. Mangano, *J Craniofac Surg* **2013**, *24*, 856.
[8] M. H. Helal, H. D. Hendawy, R. A. Gaber, N. R. Helal, M. N. Aboushelib, *J Prosthet Dent* **2019**, *121*, 118.
[9] M. Jacotti, C. Barausse, P. Felice, *Implant Dent* **2014**, *23*, 22.
[10] F. Mangano, A. Macchi, J. A. Shibli, G. Luongo, G. Iezzi, A. Piattelli, A. Caprioglio, C. Mangano, *J Oral Implantol* **2014**, *40*, 561.
[11] F. G. Mangano, P. A. Zecca, R. van Noort, S. Apresyan, G. Iezzi, A. Piattelli, A. Macchi, C. Mangano, *Case Rep Dent* **2015**, *2015*, 941265.
[12] C. Garot, G. Bettega, C. Picart, *Adv Funct Mater* **2021**, *31*.
[13] K. Lin, R. Sheikh, S. Romanazzo, I. Roohani, *Materials (Basel)* **2019**, *12*.
[14] P. Rider, Ž. P. Kačarević, S. Alkildani, S. Retnasingh, R. Schnettler, M. Barbeck, *Int J Mol Sci* **2018**, *19*.
[15] L. Roseti, V. Parisi, M. Petretta, C. Cavallo, G. Desando, I. Bartolotti, B. Grigolo, *Materials Science and Engineering: C* **2017**, *78*, 1246.
[16] T. Albrektsson, A. Wennerberg, *Int J Prosthodont* **2004**, *17*, 536.
[17] M. I. Gariboldi, S. M. Best, *Front Bioeng Biotechnol* **2015**, *3*, 151.
[18] F. M. Klenke, Y. Liu, H. Yuan, E. B. Hunziker, K. A. Siebenrock, W. Hofstetter, *J Biomed Mater Res A* **2008**, *85*, 777.
[19] F. Lambert, M. Bacevic, P. Layrolle, P. Schüpbach, P. Drion, E. Rompen, *Clinical Oral Implants Research* **2017**, *28*, e201.
[20] R. A. Perez, G. Mestres, *Materials Science and Engineering: C* **2016**, *61*, 922.
[21] B. De Carvalho, E. Rompen, G. Lecloux, P. Schupbach, E. Dory, J.-F. Art, F. Lambert, *Materials (Basel)* **2019**, *12*.
[22] J. Mealy, K. O'Kelly, *J Biomed Mater Res A* **2015**, *103*, 3533.
[23] M. A. Alias, P. R. Buenzli, *Biophys. J.* **2017**, *112*, 193.
[24] E. Gamsjäger, C. M. Bidan, F. D. Fischer, P. Fratzl, J. W. C. Dunlop, *Acta Biomater* **2013**, *9*, 5531.
[25] Y. Guyot, I. Papantoniou, F. P. Luyten, L. Geris, *Biomech Model Mechanobiol* **2016**, *15*, 169.
[26] M. Rumpler, A. Woesz, J. W. C. Dunlop, J. T. van Dongen, P. Fratzl, *J R Soc Interface* **2008**, *5*, 1173.

[27] M. Werner, S. B. G. Blanquer, S. P. Haimi, G. Korus, J. W. C. Dunlop, G. N. Duda, D. W. Grijpma, A. Petersen, *Adv Sci (Weinh)* **2017**, *4*, 1600347.
[28] M. Wang, N. Yang, X. Wang, *Med Biol Eng Comput* **2017**, *55*, 1895.
[29] A. Carlier, J. Lammens, H. Van Oosterwyck, L. Geris, *In Silico Cell Tissue Sci* **2015**, *2*, 1.
[30] C. Perier-Metz, G. N. Duda, S. Checa, *Front Bioeng Biotechnol* **2020**, *8*, 585799.
[31] C. Sandino, S. Checa, P. J. Prendergast, D. Lacroix, *Biomaterials* **2010**, *31*, 2446.
[32] C. Sandino, D. Lacroix, *Biomech Model Mechanobiol* **2011**, *10*, 565.
[33] M. Rubert, J. R. Vetsch, I. Lehtoviita, M. Sommer, F. Zhao, A. R. Studart, R. Müller, S. Hofmann, *Tissue Eng Part A* **2020**.
[34] L. Le Guéhennec, D. Van Hede, E. Plougonven, G. Nolens, B. Verlée, M.-C. De Pauw, F. Lambert, *J Biomed Mater Res A* **2019**.
[35] J. P. Long, S. J. Hollister, S. A. Goldstein, *J Biomech* **2012**, *45*, 2651.
[36] D. Luo, Q. Rong, Q. Chen, *Med Eng Phys* **2017**, *47*, 176.
[37] X. Luo, B. Yang, L. Sheng, J. Chen, H. Li, L. Xie, G. Chen, M. Yu, W. Guo, W. Tian, *Biomaterials* **2015**, *57*, 59.
[38] S. V. Dorozhkin, M. Epple, *Angew. Chem. Int. Ed. Engl.* **2002**, *41*, 3130.
[39] J. Jeong, J. H. Kim, J. H. Shim, N. S. Hwang, C. Y. Heo, *Biomater Res* **2019**, *23*.
[40] I. S. Harding, N. Rashid, K. A. Hing, *Biomaterials* **2005**, *26*, 6818.
[41] B. H. Fellah, O. Gauthier, P. Weiss, D. Chappard, P. Layrolle, *Biomaterials* **2008**, *29*, 1177.
[42] O. Andrukhov, R. Huber, B. Shi, S. Berner, X. Rausch-Fan, A. Moritz, N. D. Spencer, A. Schedle, *Dental Materials* **2016**, *32*, 1374.
[43] S. Van Bael, Y. C. Chai, S. Truscello, M. Moesen, G. Kerckhofs, H. Van Oosterwyck, J.-P. Kruth, J. Schrooten, *Acta Biomater* **2012**, *8*, 2824.
[44] A. Boccaccio, A. E. Uva, M. Fiorentino, G. Mori, G. Monno, *PLoS ONE* **2016**, *11*, e0146935.
[45] A. A. Zadpoor, *Biomater Sci* **2015**, *3*, 231.
[46] X. Liu, M. N. Rahaman, Q. Fu, *Acta Biomater* **2013**, *9*, 4889.
[47] J. Serrano-Bello, I. Cruz-Maya, F. Suaste-Olmos, P. González-Alva, R. Altobelli, L. Ambrosio, L. A. Medina, V. Guarino, M. A. Alvarez-Perez, *Front Bioeng Biotechnol* **2020**, *8*, 587.
[48] A. C. Jones, C. H. Arns, D. W. Hutmacher, B. K. Milthorpe, A. P. Sheppard, M. A. Knackstedt, *Biomaterials* **2009**, *30*, 1440.
[49] L. Pieuchot, J. Marteau, A. Guignandon, T. Dos Santos, I. Brigaud, P.-F. Chauvy, T. Cloatre, A. Ponche, T. Petithory, P. Rougerie, M. Vassaux, J.-L. Milan, N. Tusamda Wakhloo, A. Spangenberg, M. Bigerelle, K. Anselme, *Nat Commun* **2018**, *9*, 3995.
[50] P. Habibovic, H. Yuan, C. M. van der Valk, G. Meijer, C. A. van Blitterswijk, K. de Groot, *Biomaterials* **2005**, *26*, 3565.
[51] P. Habibovic, T. M. Sees, M. A. van den Doel, C. A. van Blitterswijk, K. de Groot, *J Biomed Mater Res A* **2006**, *77*, 747.
[52] M. Cheng, T. Wahafu, G. Jiang, W. Liu, Y. Qiao, X. Peng, T. Cheng, X. Zhang, G. He, X. Liu, *Sci Rep* **2016**, *6*, 24134.
[53] M. De Wild, C. Ghayor, S. Zimmermann, J. Rüegg, F. Nicholls, F. Schuler, T.-H. Chen, F. E. Weber, *3D Printing and Additive Manufacturing* **2018**, *6*, 40.
[54] A. A. El-Rashidy, J. A. Roether, L. Harhaus, U. Kneser, A. R. Boccaccini, *Acta Biomater* **2017**, *62*, 1.
[55] S. F. Hulbert, F. A. Young, R. S. Mathews, J. J. Klawitter, C. D. Talbert, F. H. Stelling, *J. Biomed. Mater. Res.* **1970**, *4*, 433.
[56] S. M. M. Roosa, J. M. Kemppainen, E. N. Moffitt, P. H. Krebsbach, S. J. Hollister, *J Biomed Mater Res A* **2010**, *92*, 359.
[57] I. Denry, L. T. Kuhn, *Dent Mater* **2016**, *32*, 43.
[58] A. Erdemir, L. Mulugeta, J. P. Ku, A. Drach, M. Horner, T. M. Morrison, G. C. Y. Peng, R. Vadigepalli, W. W. Lytton, J. G. Myers, *J Transl Med* **2020**, *18*, 369.

[59] P. Pathmanathan, J. M. Cordeiro, R. A. Gray, *Front Physiol* **2019**, *10*, 721.
[60] E. A. Patterson, M. P. Whelan, *Prog Biophys Mol Biol* **2017**, *129*, 13.
[61] Y. Guyot, I. Papantoniou, Y. C. Chai, S. Van Bael, J. Schrooten, L. Geris, *Biomech Model Mechanobiol* **2014**, *13*, 1361.
[62] C. M. Bidan, K. P. Kommareddy, M. Rumpler, P. Kollmannsberger, Y. J. M. Bréchet, P. Fratzl, J. W. C. Dunlop, *PLoS One* **2012**, *7*, e36336.
[63] R. Goffard, T. Sforza, A. Clarinval, T. Dormal, L. Boilet, S. Hocquet, F. Cambier, *Advances in Production Engineering & Management* **2013**, *8*, 96.
[64] C. Kilkenny, W. J. Browne, I. Cuthi, M. Emerson, D. G. Altman, *Vet Clin Pathol* **2012**, *41*, 27.
[65] F. Faul, E. Erdfelder, A.-G. Lang, A. Buchner, *Behavior Research Methods* **2007**, *39*, 175.

The table of contents

3D printing combined to in silico modelling is a promising strategy to develop synthetic calcium phosphates-based scaffolds displaying an optimized internal design for bone regenerative applications. This study validates this approach and shows that the Gyroid design is associated to a strongly enhanced bone regenerative capacity when implanted in a small animal model.

ToC figure